

# High Energy Lithium Ion Capacitors Using Hybrid Cathodes Comprising Electrical Double Layer and Intercalation Host Multi- Layers

Sang Ho Lee<sup>1,\*</sup>, Chun Huang<sup>2</sup> and Patrick S. Grant<sup>1</sup>

<sup>1</sup>Department of Materials, University of Oxford, Oxford OX1 3PH, UK.

<sup>2</sup>Department of Engineering, King's College London, London WC2R 2ND, UK.

---

\* Address correspondence to [sangho.lee@materials.ox.ac.uk](mailto:sangho.lee@materials.ox.ac.uk)

## **Abstract**

The ability to recharge and to deliver high capacity quickly is required for the next generation of lithium ion storage technologies, especially for pure electric vehicles. A new type of hybrid positive electrode for lithium ion capacitors is investigated that comprises discrete layers of high power capacitive activated carbon and high capacity insertion-type  $\text{LiFePO}_4$ , with the aim of boosting energy density towards that of a lithium ion battery while preserving capacitor-like power capability over thousands of charge/discharge cycles. The electrochemical performance of these hybrid electrodes was investigated both as a function of the  $\text{LiFePO}_4$  weight fraction (its thickness in the multi-layered electrode arrangement) and its location within the multi-layer. The best performing hybrid positive electrode architecture delivered an attractive balance of an energy density of  $\sim 90 \text{ Wh/kg}$  and a power density of  $\sim 15 \text{ kW/kg}$  in a full lithium ion capacitor configuration, which outperformed other combinations of the same materials. The ability to produce a double-sided configuration of the hybrid layered electrode over  $20 \times 20 \text{ cm}^2$  was demonstrated, confirming the potential scalability of layer-by-layer manufacture.

## **Keywords**

Hybrid electrode, layer-by-layer spray printing, activated carbon,  $\text{LiFePO}_4$ , lithium ion capacitor.

## 1. Introduction

The lithium ion battery (LIB) has come to dominate the portable energy storage market and is the currently preferred enabling technology for the electric vehicle market because of its high gravimetric and volumetric energy density ( $\sim 250$  Wh/kg and  $\sim 650$  Wh/L, respectively), comparatively high cell voltage ( $\sim 4$  V) and cost that has reduced by a factor of 10 over the last decade.<sup>[1-4]</sup> However, despite their many positive attributes, LIBs have relatively poor power capability (200-300 W/kg) and its full-charge capacity is degraded markedly after  $\sim 500$  charge/discharge cycles.<sup>[5-7]</sup>

As an alternative to LIBs for high power applications, lithium ion capacitors (LICs) have been developed that use a combination of an insertion-type negative electrode and a capacitive-type positive electrode.<sup>[8-11]</sup> The intention is to combine the best of electrochemical capacitors (ECs) and LIBs while avoiding combining their disadvantages and limitations. However in practice, LIC performance tends to be close to an average of LIB and EC behaviors e.g. a sustainable power capability ( $\sim 10$  kW/kg) that is two orders of magnitude greater than LIBs but with a reduction of energy density to typically  $\sim 30$  Wh/kg. The limited gravimetric capacity arises predominately because of the electrical double layer energy storage mechanism at the activated carbon (AC) positive electrode, which is comparatively fast but only utilizes the surface area of the active material rather than its volume.<sup>[12-14]</sup> Thus, there remains a need to develop LICs with a less-compromised balance between power and energy density and that better preserves power and cycle performance without a significant sacrifice in energy density.

We have developed an electrode manufacturing approach based on spray printing with many similarities to the conventional slurry casting process that is

used widely to fabricate the electrodes for LIBs and LICs, but which also allows the fabrication of novel electrode architectures using conventional and novel energy storage materials. The process provides greater control over the arrangement of electrode materials during electrode formation and drying, which has been shown to produce marked performance improvements and to deliver extra functionality for lithium-based energy storage applications. For instance, hard-to-process honeycomb structures have been fabricated spontaneously over large areas of current collectors by combining spray printing with a bi-solvent drying approach, which has been exploited for a diverse range of active materials such as  $\text{TiO}_2(\text{B})$ , carbon nanofibers, graphene, AC and  $\text{LiFePO}_4$  (LFP), in every case boosting electrode reaction kinetics at ultra-fast charging rates.<sup>[15-18]</sup> The spray printing process also allows for the fabrication of multi-layered LIB electrode configurations, as the electrode is formed from many sub-layers, layer-by-layer, and each layer can in principle be different in compositions to preceding or subsequent layers. For example, two layer electrodes comprising a porous  $\text{TiO}_2$  layer (next to the current collector) and a non-porous  $\text{TiO}_2$  (adjacent to the separator/cathode) showed improved ion mobility and volumetric capacity,<sup>[19]</sup> while interleaving Si/ $\text{SiO}_x$  nanocomposite layers between two layers of conductive carbon reduced interfacial resistance at the electrode/current collector and avoided pulverization of the Si/ $\text{SiO}_x$ .<sup>[20]</sup> Recently, high power  $\text{Li}_4\text{Ti}_5\text{O}_{12}$  (LTO) and high capacity Si were spray printed, layer-by-layer, into a multi-layered configuration for high power LIB applications.<sup>[21]</sup>

In this paper, novel LIC positive electrode architectures are manufactured through the multi-layer printing of discrete layers of insertion-type LFP and capacitive AC particulates, layer-by-layer, into a single electrode structure. The



electrochemical behavior of these hybrid electrodes is investigated first as a function of the LFP weight fraction from 0 to 100 wt% and then as a function of the LFP position in different multi-layer architectures. The optimum fraction and discrete location of the LFP layer within the AC-based electrode gave an energy density of  $\sim 90$  Wh/kg and a power density of  $\sim 15$  kW/kg, which were at least double that of conventional LIC arrangements. The hybrid LIC positive electrode was successfully scaled-up to areas of  $20 \times 20$  cm<sup>2</sup> in a double-sided electrode configuration.

## 2. Results and discussion

Figure 1 shows schematically the approach for the fabrication of hybrid LIC positive electrodes involving the spray printing of discrete, sequential layers based on capacitive AC and faradaic LFP. Spray printing is a versatile deposition technique that involves the compressed gas atomization of a relatively low viscosity liquid suspension of solid particulates, based on conventional slurry casting formulations, and the projection of the resulting suspension droplets onto a heated current collector. The electrode forms incrementally layer-by-layer through iterations of the spray pattern over the substrate. An aqueous-based bi-solvent was used to form the stable suspensions, based on 40 vol% isopropyl alcohol (IPA) and 60 vol% deionized water (DI) for both AC and LFP based suspensions. Both suspensions also contained Super P (SP) carbon as an electrical conductivity enhancer and carboxymethyl cellulose (CMC) as a binder. The current collector foil on the heated vacuum chuck promoted fast drying of deposited suspension droplets so there was no excessive IPA/DI build-up and only limited transitory inter-mixing between layers as the electrode structure evolved. Discrete layers of AC and LFP within the electrode were achieved simply by switching atomization between the AC or LFP containing feedstock suspensions at will. Final electrode thicknesses can be controlled, from a few microns up to hundreds of microns, by changing the number of spray scan cycles and/or the solid fraction of the feedstock suspensions.

The multi-layered and hybrid electrode configuration aimed to exploit the fast electrode kinetics of the electrical double layer mechanism (AC) and the capacity benefits of the intercalation reaction (LFP) simultaneously in a single electrode, as described in the magnified cartoon in Figure 1. It was anticipated that too small fractions of LFP in the electrode would make little difference to energy density,

while on the other hand a high fraction of LFP would deliver useful LIB-like capacity only at relatively low charge/discharge rates. Thus, the hypothesis to be investigated was that an attractive balance of capacity and power could be provided at an optimum LFP and AC fraction, and that this balance would be most advantageously realized as a discrete layer of LFP in AC, rather than by a simple random mixture of the two active materials.

Figures 2a-d show a series of scanning electron microscope (SEM) images of multi-layered electrode cross-sections with varying LFP fraction (directly related to the LFP-based layer thickness), where the discrete LFP layer was located at the base of the electrode layers, i.e. next to the Al current collector. All electrodes comprised commercial particulates of  $\sim 10\ \mu\text{m}$  AC and  $\sim 5\ \mu\text{m}$  LFP (more detailed images of the AC and LFP are given in Figure S1 of the Supporting Information). As the LFP fraction increased in the range of 10 to 80 wt% and correspondingly the AC fraction decreased from 90 to 20 wt%, as delineated by the red dotted lines, the overall electrode thicknesses decreased slightly, from 80 to 74  $\mu\text{m}$ , because of the different packing densities of AC and LFP, as given in Table 1. Figure S2 in the Supporting Information shows the surface of the sprayed electrodes. Figure 2e magnifies the region of the AC/LFP sub-layer interface, suggesting a comparatively high porosity fraction of the AC layer (estimated at approximately 60 %) that may be helpful in promoting the mobility of active lithium ions into the “lower” LFP layer. Figures 2f-h show a series of energy-dispersive X-ray spectroscopy (EDS) elemental maps of the layered electrode containing 20 wt% LFP. The discrete layers of AC and LFP are clearly discriminated, for example by the Fe map, indicating there was only limited re-suspension and inter-mixing of pre-formed layers at the

interface between AC and LFP layers (see the more detailed elemental maps in Figure S3 of the Supporting Information).

The electrochemical behavior of the hybrid electrodes was investigated in half-cell configurations as a function of the LFP fraction. Figure 3a shows cyclic voltammetry (CV) profiles at a constant scan rate of 0.1 mV/s. As the LFP fraction increased progressively, the peak current density at approximately 3.6 V (the anodic sweep) and 3.3 V (the cathodic sweep) increased markedly. These intercalation reactions obscured the lower energy density electrical double layer formation that can be seen in the magnified inset figures with a characteristic near-rectangular CV shape. As expected, the predominant energy storage mechanism changed progressively from the capacitive electrical double layer mechanism to the intercalation mechanism as the LFP fraction increased. Figure 3b shows gravimetric charge/discharge plots at 20 mA/g as a function of the LFP fraction. The AC-only electrode showed a near linear response typical of capacitive energy storage. As the LFP fraction increased, characteristic voltage plateaus between 3.3 to 3.5 V appeared and were progressively extended.

Figure 3c shows the gravimetric discharge profiles of the identical half-cell electrodes at increasing charge/discharge current densities from 20 to 8000 mA/g. At relatively low current densities of 20 to 200 mA/g, the LFP-only electrode delivered the highest capacity as expected, while the AC-only had the lowest capacity. In the AC/LFP hybrid electrodes, with increasing LFP fraction, capacity improvements were marked only at the low current densities, and reduced rapidly as current densities increased to 8000 mA/g. Eventually, at 8000 mA/g the hybrid electrode containing 20 wt% LFP had the highest capacity that was twice that of the AC-only, while the LFP-only and 80 wt% LFP electrodes had almost no useful

residual capacity (see Table 1). Figure S4 of the Supporting Information shows the electrode coulombic efficiency. As LFP fraction increased, initial coulombic efficiency decreased due to irreversible surface reactions commonly seen for LIBs in the first few cycles. However, excluding the first few cycles the electrodes had a coulombic efficiency close to 100 %.

Figure 3d shows the corresponding Nyquist plots where the AC-only electrode had the lowest charge transport resistance, which was indicated by the smaller diameter best-fit semi-circle. As the LFP fraction increased, the diameter increased progressively, indicating a monotonic increase in electrode resistance with LFP fraction. The Warburg impedance for the AC-only electrode was close to vertical (near pure capacitance), however, as LFP fraction increased, the Warburg impedance gradient gradually decreased. Overall, these data show a consistent trend of higher capacity but higher resistance at low current densities and high LFP fractions, and the inverse trend as the more conductive, more responsive AC fraction increased.

The different AC/LFP hybrid electrodes were then investigated as positive electrodes when coupled with spray printed LTO negative electrodes in a full LIC configuration, as depicted schematically in the inset of Figure 4a (please refer to half-cell performances of the spray printed LTO electrode in Figure S5 and Table S1 of the Supporting Information). We present data for a 1:2 anode:cathode mass ratio to balance power and capacity. However, Figure S6 in the Supporting Information also shows comparative performance of LICs with 1:2 and 1:3 ratios, where the increasing ratio promoted higher energy density but decreased in power density. Figure 4a shows the Ragone plots for the full LICs as a function of the LFP fraction in the hybrid positive electrode. The specific power  $P$  and energy  $E$  density

were estimated using  $P \text{ [W/kg]} = V \times i/m$  and  $E \text{ [Wh/kg]} = P \times t$ , where  $V \text{ [V]}$  was the average cell potential between the highest and lowest cut-off voltage,  $i \text{ [A]}$  was the current,  $m \text{ [kg]}$  was the total mass of both negative and positive electrodes including LTO, AC, LFP, SP and CMC, and  $t \text{ [h]}$  was the charging time.<sup>[22,23]</sup> At 20 mA/g, the AC-only-based LIC delivered an energy density of  $\sim 40 \text{ Wh/kg}$ , much lower than the LIB configuration with a LFP-only electrode of  $\sim 190 \text{ Wh/kg}$ . As LFP fraction increased from 10 to 80 wt% in the hybrid AC/LFP cathodes, the LIC specific energy at 20 mA/g increased from 65 to 140 Wh/kg. However, as charging rates increased progressively, LICs containing higher fractions of LFP (e.g. 40 and 80 wt%) showed a rapid decrease in deliverable power, similar to that of the LIB configuration. The hybrid electrode containing 20 wt% LFP had the best overall energy and power performance when compared with the “pure” LIC configuration (LTO || AC-only), with a specific energy density of  $\sim 85 \text{ Wh/kg}$  and a specific power density of  $\sim 7000 \text{ W/kg}$ .

Figure 4b shows discharge curves at 2 A/g for the LICs as a function of LFP fraction (also see the corresponding charge curves in the inset). Capacitance  $C \text{ [F/g]}$  was estimated using  $C = i \times t/V$ , where  $i \text{ [A/g]}$  was the applied current based on the total mass of both anodes and cathodes including LTO, AC, LFP, SP and CMC,  $t \text{ [s]}$  was the discharge or charge time, and  $V \text{ [V]}$  was the potential difference.<sup>[24,25]</sup> At 2 A/g, the LIC with a 20 wt% LFP positive electrode had a higher capacitance ( $\sim 100 \text{ F/g}$ ) than the AC-only ( $\sim 50 \text{ F/g}$ ), both of which were superior to 80 wt% LFP ( $\sim 40 \text{ F/g}$ ). LFP is more energy dense than AC because the volume of the material can contribute to storage capacity whereas AC stores ions only at the surface, and the AC-only electrode therefore had the lowest gravimetric capacity, as shown in Figure 3c. At 10 and 20 wt% LFP in an otherwise AC electrode, overall

electrode capacity increased and the response remained “capacitor-like” with a broadly near-linear potential versus time discharge plot in Figure 4b. However, above 20% LFP the electrode became too “battery-like”, with sluggish kinetics, and useful capacity faded at higher rates.

Figures 4c-d show LIC cycle stability as a function of LFP fraction. As charge/discharge cycles continued to the 1000<sup>th</sup> cycle at 200 mA/g, the energy density of the 80 wt% LFP positive electrode declined rapidly to ~ 30 Wh/kg (~ 35 % energy density retention), becoming almost similar to the AC-only electrode. However, the energy density reduction of 10 and 20 wt% LFP positive electrodes was less marked, even after 1000 cycles, with stable energy densities of ~ 45 Wh/kg and ~ 65 Wh/kg, respectively (~ 85 % energy density retention for both positive electrodes).

A second optimization investigated the possibility of realizing further performance benefits in hybrid electrode systems by varying the location of the best performing 20 wt% LFP layer, as shown in the series of electrode cross-section SEM images in Figures 5a-c: (a) LFP next to the current collector as previously described (denoted as LFP-AC hereafter); (b) between two layers of AC (AC-LFP-AC); and (c) on the top of the AC, closest to the separator and negative electrode (AC-LFP). The left upper cartoons schematically indicate these configurations. The right-hand insets magnify the region containing the LFP layer in the hybrid electrode. Figures 5d-f show the corresponding EDS maps for Fe (orange), confirming the discrete LFP locations. The thickness of the discrete layers of AC and LFP in each hybrid electrode was consistently maintained, as quantified in Table 2.

Figure 6a shows the gravimetric half-cell performance data as a function of the LFP location (also see corresponding volumetric performance in Figure S7 of the Supporting Information that was estimated by normalizing the gravimetric data by the electrode mass and thickness, given in Table 2). At a relatively low current density of 20 mA/g, the three electrodes had an almost similar capacity of  $\sim 75$  mAh/g regardless of the LFP location because there was sufficient time for active ions to move throughout the tortuous inter-connected pore network and reach active sites for storage reactions for all arrangements. Under these conditions, LFP provided the dominant contribution to capacity. As the current density increased to 8000 mA/g, the LFP location markedly affected electrode capacity. At 8000 mA/g, the AC-LFP configuration had the highest discharge capacity of  $\sim 45$  mAh/g, representing  $\sim 75$  % improvement in the deliverable capacity over the LFP-AC electrode ( $\sim 26$  mAh/g) and four times that of the AC-only electrode ( $\sim 11$  mAh/g).

For a full LIC configuration in the Ragone plots in Figure 6b, as the LFP layer was positioned closer to the LTO negative electrode, the LIC power density increased. Consequently, a LIC using an AC-LFP electrode improved LIC performance balance further, giving a high energy density of  $\sim 90$  Wh/kg at  $\sim 15$  W/kg and a power density of  $\sim 15$  kW/kg even at an energy density of  $\sim 45$  Wh/kg. Compared with a capacitive AC-only electrode, capacity and power were both approximately doubled. The scheme in the inset describes the best performing LIC arrangement.

Figure 6c shows the galvanostatic energy density profiles at a constant current density of 1000 mA/g for LIC cells using the AC-LFP and AC-only positive electrodes. After 2000 cycles, the AC-LFP and AC-only electrodes delivered  $\sim 55$  Wh/kg and  $\sim 25$  Wh/kg, respectively, indicating  $\sim 75$  % and  $\sim 85$  % energy density



retention, respectively, as shown in the right-hand inset. The relatively rapid decline in the energy density retention of the AC-LFP-based LIC was presumably associated with some pulverization of the LFP, despite its comparatively low insertion strain and high rate tolerance.<sup>[26-28]</sup> The photograph in the left-hand inset shows a double-sided spray printed AC-LFP hybrid electrode over a 20 cm × 20 cm Al foil. The scalable, double-sided electrode demonstration suggests scalability for multi-layer electrode pouch cell packs for automotive applications.

To assess any benefits of the layering itself, spray printed electrodes comprising randomly mixed AC and LFP particulates in the same 80 wt% AC and 20 wt% LFP combination were fabricated. Figure S8 in the Supporting Information exhibits a series of SEM electrode cross-sections images of the (a) AC-only, (b) AC-LFP multi-layer, (c) random-mix and (d) LFP-only electrodes. Figure S9a shows their corresponding half-cell CV curves at 0.1 mV/s. As before, there were two strong peaks at approximately 3.6 V (the anodic sweep) and 3.3 V (the cathodic sweep) for the layered and random-mix electrodes due to the lithium ion intercalation reaction of LFP, and there were distinct voltage plateaus at 3.4 V for the same electrodes in the potential-capacity plots in Figure S9b. Figure S9c shows the half-cell capacity at increasing current densities of 20 to 8000 mA/g, noting that electrode mass was almost same for all the electrodes (see Table S2 in the Supporting Information). The layered electrode outperformed the random-mix electrode in terms of discharge capacity at all rates (while the random-mix electrode had higher capacity than the AC-only electrode), confirming that the beneficial addition of 20 wt% LFP was realized more markedly when used as a discrete layer. Figure S9d shows the Ragone plots for LICs utilizing the layered, random-mix and

AC-only positive electrodes, supporting the superiority of the layered electrode structure in terms of LIC energy and power performance.

To understand why the AC-LFP electrode configuration had superior energy storage performance at intermediate and high charge/discharge rates, the effective lithium ion mobility within the LFP part of the positive electrode was estimated for each of LFP locations. Figures 7a-c exhibit CV curves at increasing scan rates of 0.05 to 2.00 mV/s for a series of multi-layered electrodes with different LFP locations, as shown in the cartoons in the lower insets. As the LFP layer was located further away from the current collector, correspondingly closer progressively to the negative electrode, cathodic and anodic sweep peak current densities increased as the scan rate increased. The AC-LFP electrode had the highest anodic/cathodic peak current density at 2 mV/s. The upper insets in Figures 7a-c show plots of the anodic peak current density at approximately 3.7 V as a function of the square root of the scan rate for each electrode. The current density trend showed a good linear-fit relation to the square root of the scan rate in each case so that the effective lithium ion mobility in the LFP layer could be estimated from the Randles-Sevcik equation:<sup>[29,30]</sup>

$$I_p = 0.4463n F A C_0 (n F v M_{Li} / RT)^{1/2} \quad (1)$$

where  $I_p$  [A] was the peak current,  $n$  was the number of electrons transferred,  $F$  [C/mol] was the Faraday constant,  $A$  [cm<sup>2</sup>] was the effective electrode area,  $C_0$  [mol/cm<sup>3</sup>] was the molar concentration of the lithium ions in the electrode,  $v$  [V/s] was the CV scan rate,  $M_{Li}$  [cm<sup>2</sup>/s] was the effective lithium ion mobility,  $R$  [J/K·mol] was the Gas constant and  $T$  [K] was temperature. The Randles-Sevcik is generally

applied to uniform composition electrodes, not layered electrodes, but nonetheless can give a useful estimate of the effective mobility of ions in any diffusion-controlled electrode response. The effective ion mobility is well-known to be sensitive to electrode microstructure,<sup>[31-33]</sup> which is the principal variable of interest here. Because we carefully ensured that the electrode mass loadings and compositions in the layered electrode were the same (Figure 5 and Table 2), it is a reasonable assumption that any change in electrode performance likely related to changes in the ion mobility in the significantly varied microstructures, i.e. due to changes in the LFP location.

The bar graphs in Figure 7d show the arising estimates of the effective lithium ion mobility. When the LFP layer was close to the negative electrode and furthest from the current collector, the mobility was at a maximum of  $\sim 6.9 \times 10^{-11} \text{ cm}^2/\text{s}$ , which was 25 % higher than that of the LFP-AC configuration (LFP furthest from the negative electrode,  $M_{\text{Li}} \sim 5.5 \times 10^{-11} \text{ cm}^2/\text{s}$ ), even though they had the same microstructure.

As the charge/discharge rate is increased, a gradient in the concentration of active ion charge carriers develops through the thickness of the hybrid electrode: regions closest to the separator/anode tend to have higher concentrations compared with more distant region close to the current collector. Because the LFP charge storage mechanism involves intercalation reactions that can involve all the LFP “volume” and a comparatively large number of ions, when there is an ion concentration gradient, the LFP layer is more sensitive to its location in this gradient. Conversely, the AC layer(s) requires only sufficient ions to cover the available electro-active “surface”, which can be achieved relatively quickly. The more efficient use of available ions by the LFP when it is adjacent to the separator

is indicated by the higher ion mobility (derived from the intercalation current density) measured for this configuration (Figure 7a). The importance of the LFP location is also shown by the better rate performance of the AC-LFP layered electrode when compared with the otherwise random-mix electrode with the LFP scattered across the electrode. A further beneficial, super-imposed effect is the reduction in the electronic charge transfer resistance provided by placing the AC, with higher intrinsic electrical conductivity, layer directly on the current collector.

Previous studies of mixed active materials in LIC positive electrodes, e.g. AC/LiMn<sub>2</sub>O<sub>4</sub>, AC/LiCoO<sub>2</sub> and AC/LiFePO<sub>4</sub><sup>[34-36]</sup> used in randomly mixed electrodes prepared by slurry casting, and similarly to the current work, identified optimum active material ratios. Although other configurations were theorized, they could not be achieved in practice. Now, using the extra flexibility provided by the spray printing approach, we have shown that further benefits can be achieved in the AC/LiFePO<sub>4</sub> system by layering, and by locating the layers in regions of the electrode that take best advantage of the local ion concentrations, which vary spatially, most notably when charge/discharge rates (or current densities) increase.

Finally, the energy-power response of the best performing AC-LFP hetero-electrode was compared with other LTO || AC-based LIC systems in Figure 7e. LIC arrangements in the literature generally relied on higher fractions of inactive components ( $\geq 20$  wt%) than used in the current work, to promote high rate capability and extended cycle life, although the associated increase in parasitic mass of these inactive components was generally not taken into account in the gravimetric energy and power performance estimation.<sup>[17,36-40]</sup> Despite accounting for all the mass of all electrode constituents in the current work, our hybrid electrode

outperformed the other LIC configurations in terms of both energy and power density.

### 3. Conclusions

A hybrid LIC positive electrode design incorporating both a well-known intercalation host (LFP for high capacity) and a high surface area electrical double layer former (AC for fast electrode kinetics and stable cycle life) was realized by spray printing of LFP and AC into a multi-layered hetero-structure. To achieve the best balance of capacity and sustainable power, the optimum weight fraction of the discrete LFP layer and its most effective location within a multi-layered positive electrode were investigated in both half-cells and full LIC arrangements. A hybrid layered arrangement comprising a 20 wt% LFP on the top of a pre-deposited AC layer (LFP closest to the negative electrode) realized the LIC concept more fully, with a high energy density of  $\sim 90$  Wh/kg and power density of  $\sim 15$  kW/kg that outperformed conventional LICs. The hybrid structure was also trivially demonstrated over larger electrode areas of  $20\text{ cm} \times 20\text{ cm}$  in a double-side electrode configuration. This work suggests a broader potential for spray printing or other techniques for hetero-electrode fabrication where spatial control over the distribution of complementary active materials can be used to place them at electrode positions and in fractions that best match their intrinsic capabilities to the local ion environment.

#### 4. Material and methods

*Materials:* AC (YP-50F) was obtained from Kuraray, Japan; LFP from Hydro-Québec, Canada; SP from MTI Corporation, USA; and LTO and CMC from Sigma Aldrich, UK.

*Spray printed electrodes:* For the suspensions, the active material (AC, LFP or LTO), SP and CMC in a controlled mass ratio of 90:5:5, which was chosen to minimize inactive constituents, were suspended in a 60:40 bi-solvent mixture (by volume) of DI and IPA using ultra-sonication. Here, IPA was required to disperse SP and AC into an aqueous suspension with long term stability and no sedimentation. Prior to spray printing of an electrode, a current collector foil (Cu for anodes and Al for cathodes) was placed on a vacuum chuck that was then heated to a pre-set temperature of 120 °C. The sufficiently dilute suspension ( $\sim 3 \times 10^{-3}$  g/mL) of electrode constituents was then pumped to a spray nozzle and subsequently atomized by compressed air at 40 kPa, while the spray nozzle reciprocated over the foil at a constant  $z$  distance in a pre-programmed path in the  $x$  and  $y$  plane for multiple cycles. All spraying processes were conducted in a well-ventilated fume cupboard. For SEM measurements, thoroughly dried electrodes were processed by a PECS milling to investigate the morphology of the electrode cross-sections. SEM and EDS elemental map images were then taken at 5 keV in a Zeiss Merlin Analytical SEM without platinum pre-coating.

*Electrochemical testing:* The electrochemical behavior of the various layered positive electrodes was examined first in half-cells with commercial purity lithium chips (MTI, USA) that were used as a counter/reference electrode and then in LIC configurations combined with spray printed LTO negative electrodes. Note that anode-to-cathode mass ratios in LIC arrangements were fixed at 1:2 for all cases,

and all LIC cells were manufactured without a pre-lithiation process. In coin cells (CR2032), anodes and cathodes were electrically separated by a polypropylene separator (Celgard 2400, UK) that was soaked into 1 M  $\text{LiPF}_6$  electrolyte solution in a 1:1 mixture (by volume) of ethylene carbonate and dimethyl carbonate (Sigma Aldrich, UK). Charge/discharge tests were carried out at room temperature using Arbin BT2000 battery cyclers. CV measurements were conducted using Gamry 600 potentiostats. Electrochemical impedance spectroscopy (EIS) was conducted after the first three CV cycles, and the EIS frequency was controlled in the range of 1 MHz to 0.1 Hz.



## Acknowledgments

This work was supported by (1) Innovate UK grant number 102655 “ALICE – Advanced Lithium Ion Capacitors and Electrodes”, (2) the UK Engineering and Physical Science Research Council through Grant EP/M009521/1 “Enabling Next Generation Li-ion Batteries”, and (3) the UKRI EPSRC grant EP/S001239/1. The authors would like to thank Hydro-Québec for providing LFP.

## References

- [1] Z. Qi, J. Tang, S. Misraa, C. Fan, P. Lu, J. Jian, Z. He, V. G. Pol, X. Zhang, H. Wang, *Nano Energy* 69 (2020) 104381.
- [2] X. –G. Yang, G. Zhang, S. Ge, C. –Y. Wang, *PNAS* 115 (2018) 7266-7271.
- [3] M. Winter, B. Barnett, K. Xu, *Chem. Rev.* 118 (2018) 11433-11456.
- [4] X. Zhou, L. Yu, X. –Y. Yu, X. W. Lou, *Adv. Energy Mater.* 6 (2016) 1601177.
- [5] V. J. Ovejas, A. Cuadras, *Sci. Rep.* 9 (2019) 14875.
- [6] M. Li, J. Lu, Z. Chen, K. Amine, *Adv. Mater.* 30 (2018) 1800561.
- [7] A. I. Inamdar, R. S. Kalubarme, J. Kim, Y. Jo, H. Woo, S. Cho, S. M. Pawar, C. –J. Park, Y. –W. Lee, J. I. Sohn, S. Cha, J. Kwak, H. Kim, H. Im, *J. Mater. Chem. A* 4 (2016) 4691-4699.
- [8] G. Li, Z. Yang, Z. Yin, H. Guo, Z. Wang, G. Yan, Y. Liu, L. Li, J. Wang, *J. Mater. Chem. A* 7 (2019) 15541-15563.
- [9] J. Ding, W. Hu, E. Paek, D. Mitlin, *Chem. Rev.* 118 (2018) 6457-6498.
- [10] P. Han, G. Xu, X. Han, J. Zhao, X. Zhou, G. Cui, *Adv. Energy Mater.* 8 (2018) 1801243.

- [11] X. Yu, C. Zhan, R. Lv, Y. Bai, Y. Lin, Z. -H. Huang, W. Shen, X. Qiu, F. Kang, *Nano Energy* 15 (2015) 43-53.
- [12] Y. Hao, S. Wang, Y. Shao, Y. Wu, S. Miao, *Adv. Energy Mater.* 10 (2020) 1902836.
- [13] F. Sun, J. Gao, Y. Zhu, X. Pi, L. Wang, X. Liu, Y. Qin, *Sci. Rep.* 7 (2017) 40990.
- [14] T. Zhang, F. Zhang, L. Zhang, Y. Lu, Y. Zhang, X. Yang, Y. Ma, Y. Huang, *Carbon* 92 (2015) 106-118.
- [15] S. H. Lee, A. Mahadevegowda, C. Huang, J. D. Evans, P. S. Grant, *J. Mater. Chem. A* 6 (2018) 13133-13141.
- [16] S. H. Lee, K. Li, C. Huang, J. D. Evans, P. S. Grant, *ACS Appl. Mater. Interfaces* 11 (2019) 603-612.
- [17] S. H. Lee, C. Johnston, P. S. Grant, *ACS Appl. Mater. Interfaces* 11 (2019) 37859-37866.
- [18] J. Bu, P. Leung, C. Huang, S. H. Lee, P. S. Grant, *J. Mater. Chem. A* 7 (2019) 19094-19103
- [19] C. Huang, N. P. Young, J. Zhang, H. J. Snaith, P. S. Grant, *Nano Energy* 31 (2017) 377-385.
- [20] C. Huang, A. Kim, D. J. Chung, E. Park, N. P. Young, K. Jurkschat, H. Kim, P. S. Grant, *ACS Appl. Mater. Interfaces* 10 (2018) 15624-15633.
- [21] S. H. Lee, C. Huang, P. S. Grant, *Nano Energy* 61 (2019) 96-103.
- [22] S. He, S. Wang, H. Chen, X. Hou, Z. Shao, *J. Mater. Chem. A* 8 (2020) 2571-2580.
- [23] C. Fu, A. Mahadevegowda, P. S. Grant, *J. Mater. Chem. A* 4 (2016) 2597-2604.

- [24] Y. Sun, J. Tang, F. Qin, J. Yuan, K. Zhang, J. Li, D. –M. Zhu, L. –C. Qin, J. Mater. Chem. A 5 (2017) 13601-13609.
- [25] C. Huang, J. Zhang, H. J. Snaith, P. S. Grant, ACS Appl. Mater. Interfaces 8 (2016) 20756.
- [26] M. G. Fischer, X. Hua, B. D. Wilts, E. Castillo-Martínez, U. Steiner, ACS Appl. Mater. Interfaces 10 (2018) 1646-1653.
- [27] L. –H. Hu, F. –Y. Wu, C. –T. Lin, A. N. Khlobystov, L. –J. Li, Nat. Commun. 4 (2013) 1687.
- [28] L. –X. Yuan, Z. –H. Wang, W. –X. Zhang, X. –L. Hu, J. –T. Chen, Y. –H. Huang, J. B. Goodenough, Energy Environ. Sci. 4 (2011) 269-284.
- [29] S. H. Lee, C. Huang, C. Johnston, P. S. Grant, Electrochim. Acta 292 (2018) 546-557.
- [30] M. Fehse, E. Ventosa, ChemPlusChem 80 (2015) 785-795.
- [31] R. Liu, Y. Liu, Q. Kang, A. Casimir, H. Zhang, N. Li, Z. Huang, Y. Li, X. Lin, X. Feng, Y. Ma, G. Wu, RSC Adv. 6 (2016) 9402-9410.
- [32] Y. Zhang, Q. Fu, Q. Xu, X. Yan, R. Zhang, Z. Guo, F. Du, Y. Wei, D. Zhang, G. Chen, Nanoscale 7 (2015) 12215-12224.
- [33] R. Liu, D. Lia, C. Wang, N. Li, Q. Li, X. Lü, J. S. Spendelow, G. Wu, Nano Energy 6 (2014) 73-81.
- [34] A. Shellikeri, S. Yturriaga, J. S. Zheng, W. Cao, M. Hagen, J. A. Read, T. R. Jow, J. P. Zheng, J. Power Sources 392 (2018) 285-295.
- [35] D. Cericola, R. Kötz, Electrochim. Acta 72 (2012) 1-17.
- [36] D. Cericola, P. Novák, A. Wokaun, R. Kötz, J. Power Sources 196 (2011) 10305-10313.

- [37] H. Xu, X. Hu, Y. Sun, W. Luo, C. Chen, Y. Liu, Y. Huang, Nano Energy 10 (2014) 163-171.
- [38] D. Puthusseri, V. Aravindan, S. Madhavi, S. Ogale, Electrochim. Acta 130 (2014) 766-770.
- [39] Y. Lei, Z. -H. Huang, Y. Yang, W. Shen, Y. Zheng, H. Sun, F. Kang, Sci. Rep. 3 (2013) 2477.
- [40] A. Jain, V. Aravindan, S. Jayaraman, P. S. Kumar, R. Balasubramanian, S. Ramakrishna, S. Madhavi, M. P. Srinivasan, Sci. Rep. 3 (2013) 3002.

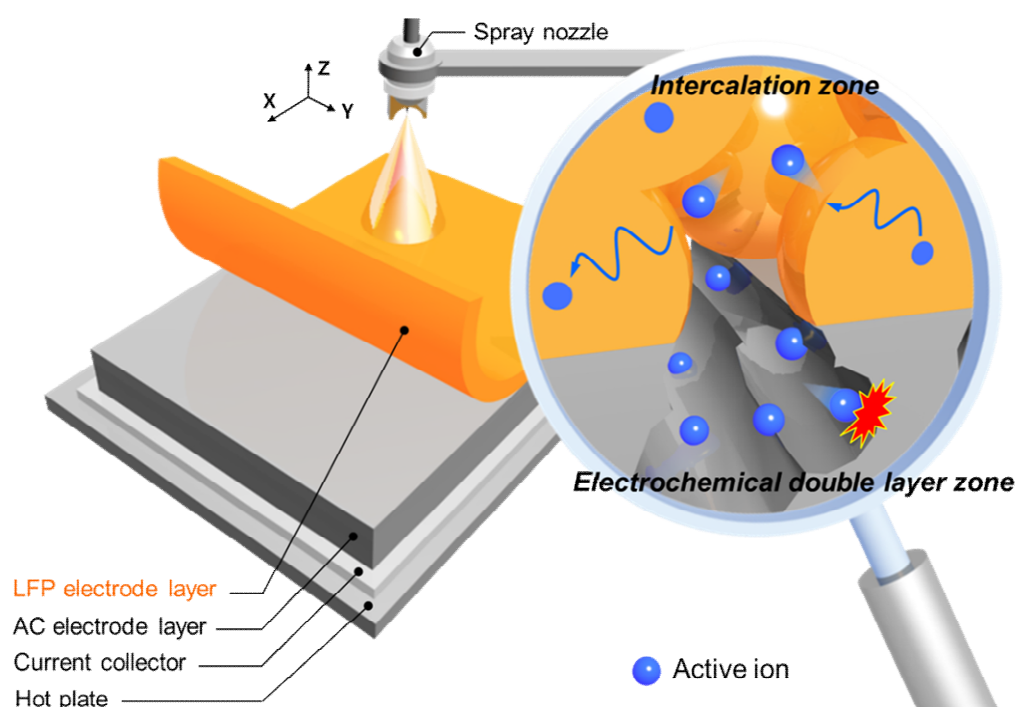


**Figure 1.** Graphical illustration of the scalable layer-by-layer printing of AC and LFP into a hybrid multi-layered positive electrode arrangement for a LIC. The magnified cartoon depicts idealized energy storage mechanisms of intercalation in LFP and electrical double layer formation on AC.

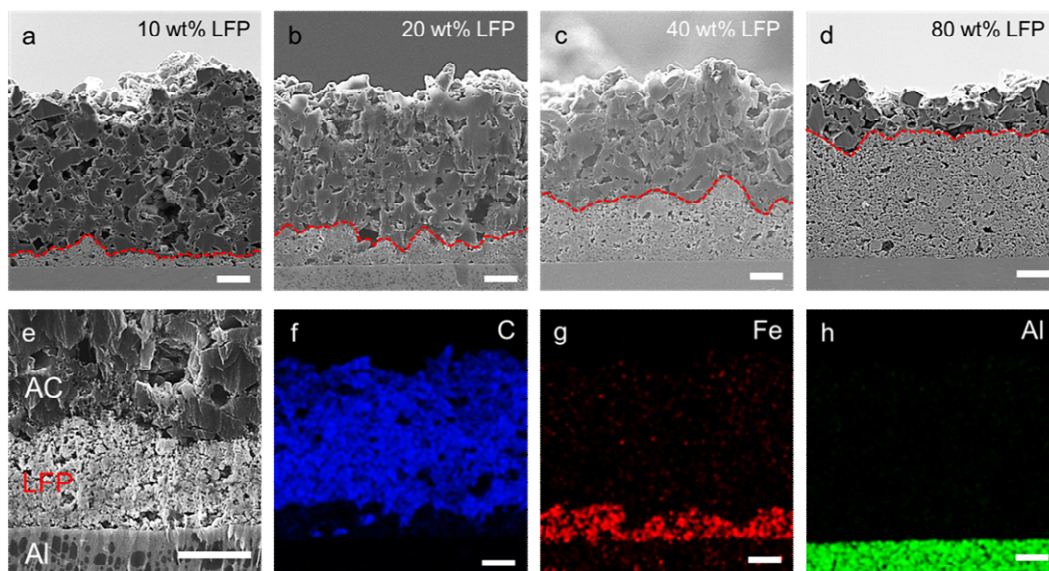


**Figure 2.** SEM images of electrode cross-sections as a function of the LFP fraction: (a) 10 wt%, (b) 20 wt%, (c) 40 wt% and (d) 80 wt% prepared using the precision etching and coating system (PECS). (e) The magnified electrode cross-section of the 20 wt% LFP layer. EDS elemental maps from the 20 wt% LFP electrode for elements: (f) C, (g) Fe and (h) Al. The scale bar indicates 10  $\mu\text{m}$ .

**Table 1.** Summary of the LIC positive electrodes with differing LFP fractions.

Electrode type	Electrode loading mass (mg/cm <sup>2</sup> )		Electrode thickness ( $\mu$ m)		Half-cell capacity (mAh/g)	
	AC	LFP	AC	LFP	20 mA/g	8000 mA/g
AC-only	7.93 $\pm$ 0.06	0	80 $\pm$ 5	0	45	11
10 wt% LFP	7.14 $\pm$ 0.05	0.78 $\pm$ 0.02	72 $\pm$ 4	7 $\pm$ 2	57	19
20 wt% LFP	6.41 $\pm$ 0.04	1.57 $\pm$ 0.04	63 $\pm$ 5	13 $\pm$ 3	74	26
40 wt% LFP	4.66 $\pm$ 0.05	3.33 $\pm$ 0.05	48 $\pm$ 5	28 $\pm$ 2	96	13
80 wt% LFP	1.58 $\pm$ 0.04	6.39 $\pm$ 0.04	17 $\pm$ 4	57 $\pm$ 2	150	6
LFP-only	0	7.92 $\pm$ 0.04	0	65 $\pm$ 3	160	0

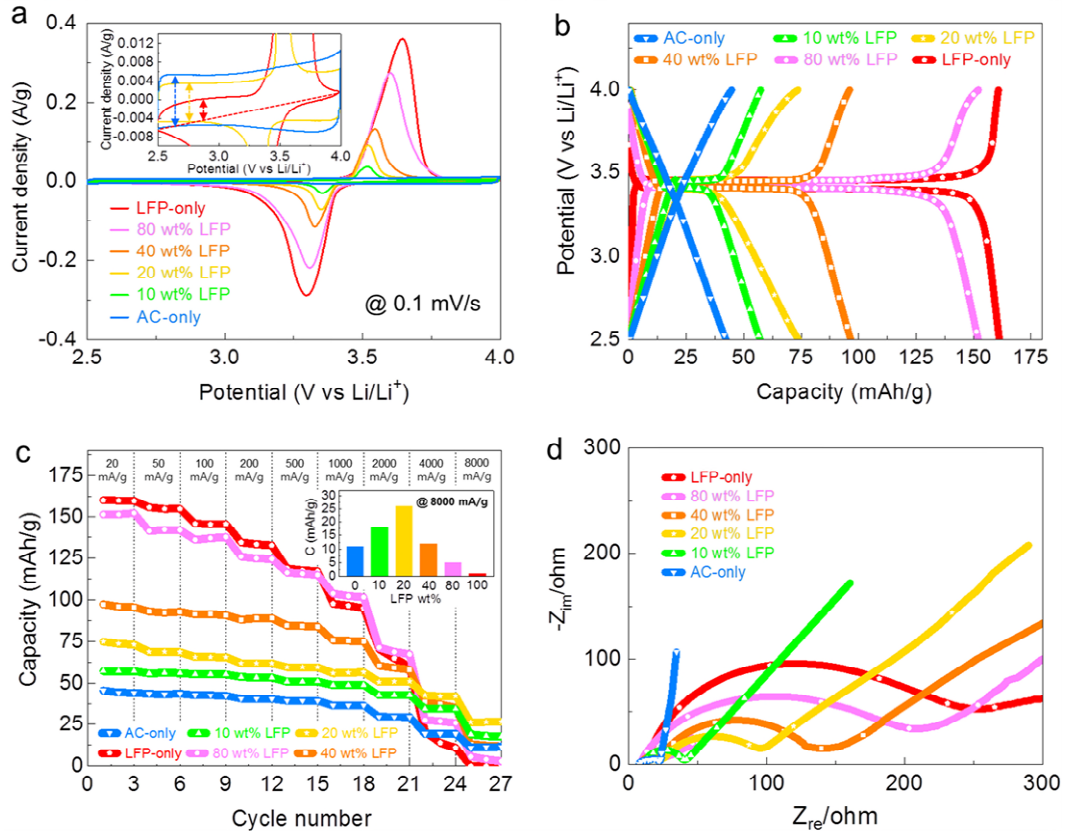


**Figure 3.** (a) CV curves for the half-cell electrodes as a function of LFP fraction at a constant scan rate of 0.1 mV/s in the potential range 2.5 to 4.0 V (vs. Li/Li<sup>+</sup>). The inset magnifies the CV plots for the AC-only, 20 wt% LFP and LFP-only electrodes. (b) Gravimetric charge/discharge plots for the electrodes as a function of the LFP fraction at a constant current density of 20 mA/g in the potential range 2.5 to 4.0 V (vs. Li/Li<sup>+</sup>). (c) Gravimetric discharge capacity profiles of the electrodes at various charge/discharge current densities in the potential range 2.5 to 4.0 V (vs. Li/Li<sup>+</sup>). The inset bar graph summarizes discharge capacities at 8000 mA/g. (d) Comparative Nyquist plots for the same electrodes.



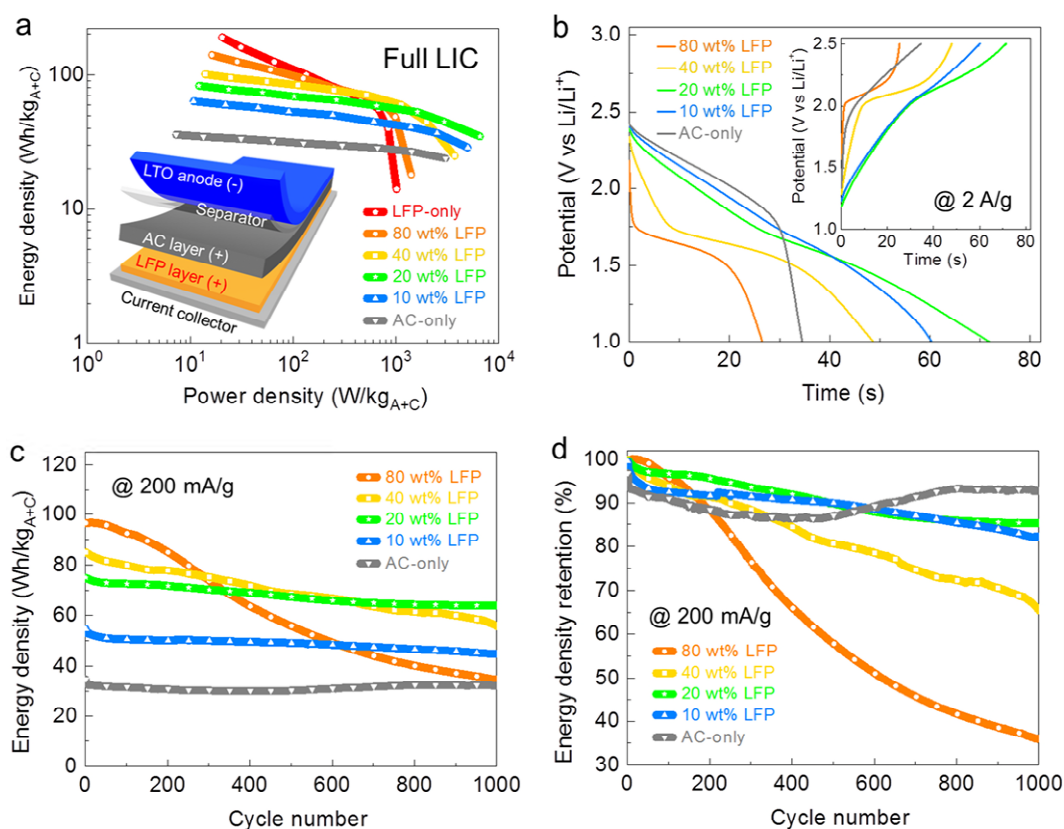


**Figure 4.** (a) Comparative LIC Ragone plots. The left corner cartoon depicts a full LIC arrangement with the AC/LFP hybrid electrode. (b) Discharge curves of LICs at 2 A/g in the potential range 1.0 to 2.5 V (vs.  $\text{Li/Li}^+$ ). The inset shows corresponding charge profiles at the same rate. (c) Galvanostatic discharge energy density profiles of LICs at a constant current density of 200 mA/g in the voltage window 1.0 to 2.5 V (vs.  $\text{Li/Li}^+$ ). (d) The corresponding energy density retention.

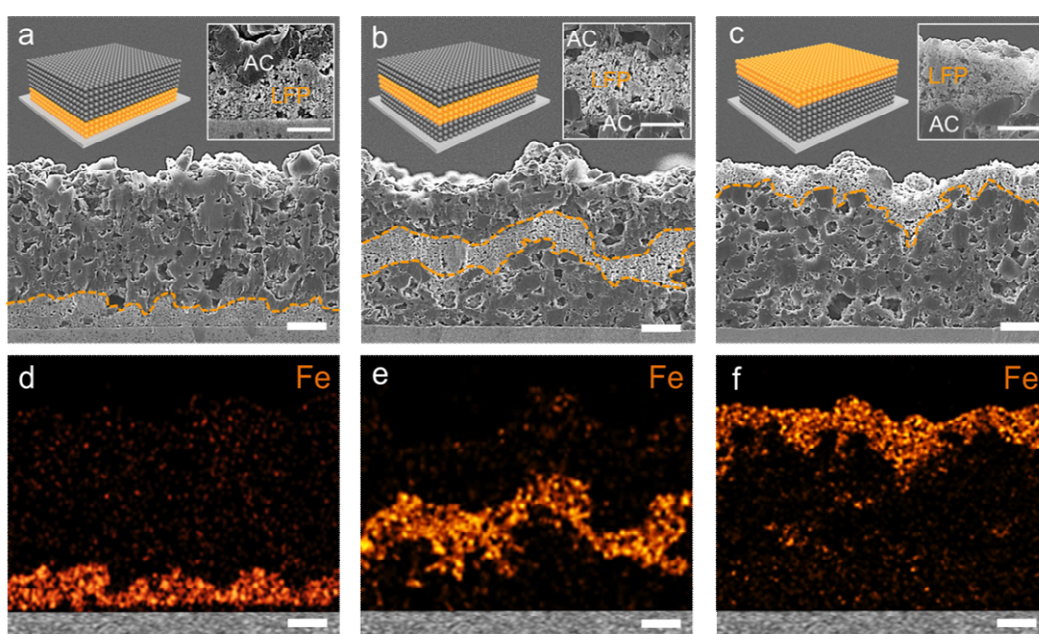


**Figure 5.** SEM images of the electrode cross-sections as a function of the LFP location that were prepared by the PECS milling: (a) LFP-AC, (b) AC-LFP-AC and (c) AC-LFP. Each of the left upper cartoons indicates the intended location of the LFP layer (orange), and the right-hand images magnify the region of the LFP layer. (d-f) EDS elemental maps for Fe (orange). The scale bar indicates 10  $\mu\text{m}$ .

**Table 2.** Summary of the hybrid electrodes as a function of the LFP location.

Electrode type	Electrode loading mass (mg/cm <sup>2</sup> )		Electrode thickness ( $\mu$ m)		Half-cell performance (mAh/g)	
	AC	LFP	AC	LFP	20 mA/g	8000 mA/g
AC-LFP	6.41 $\pm$ 0.04	1.58 $\pm$ 0.04	63 $\pm$ 5	14 $\pm$ 3	75	45
AC-LFP-AC	6.42 $\pm$ 0.03	1.57 $\pm$ 0.04	65 $\pm$ 5	13 $\pm$ 3	74	37
LFP-AC	6.40 $\pm$ 0.04	1.59 $\pm$ 0.04	64 $\pm$ 5	15 $\pm$ 3	73	26

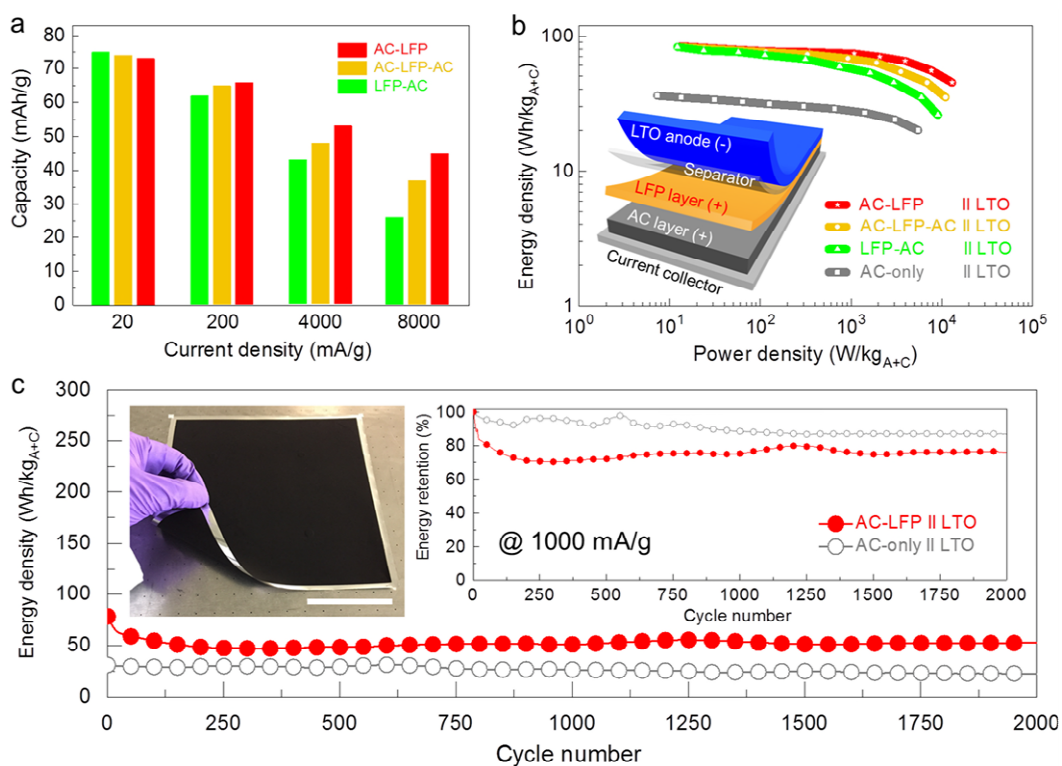


**Figure 6.** (a) Half-cell discharge capacities as a function of LFP location at increasing current densities of 20 to 8000 mA/g in the voltage window 2.5 to 4.0 V (vs. Li/Li<sup>+</sup>). (b) The LIC Ragone plots according to the variation of the LFP location in positive hybrid electrodes. The cartoon (inset) describes the best performing LIC arrangement. (c) Galvanostatic discharge energy density plot at 1000 mA/g in the voltage window 1.0 to 2.5 V (vs. Li/Li<sup>+</sup>) for LICs using the AC-only and AC-LFP electrodes. The right-hand inset shows the corresponding energy density retention. The photograph in the left-hand inset shows a spray printed double-sided AC-LFP hybrid electrode formed over a 20 cm × 20 cm Al foil. The scale bar in the photograph indicates 10 cm.

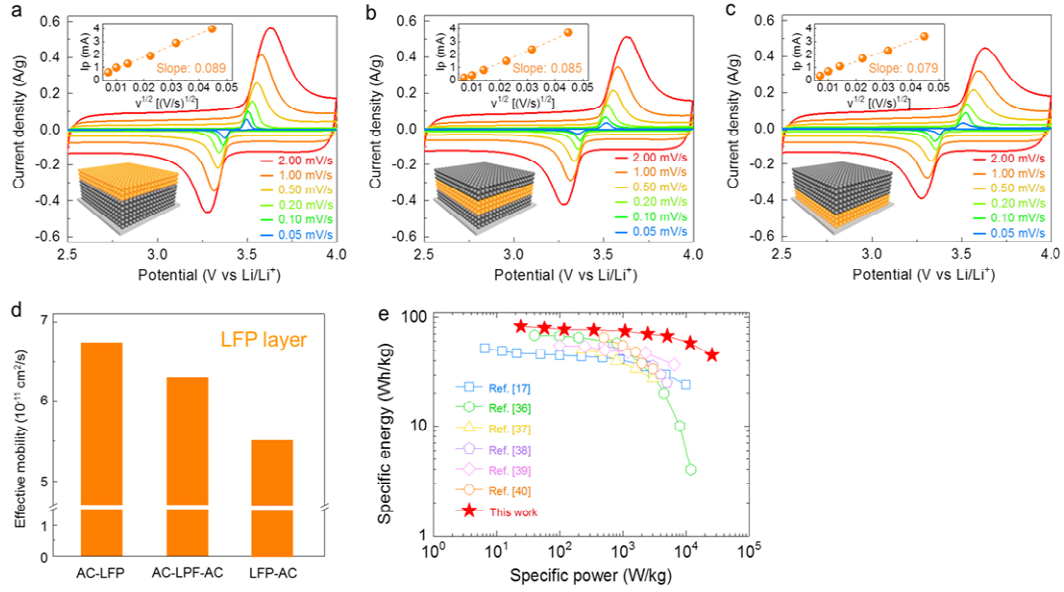


**Figure 7.** (a-c) CV profiles for the hybrid electrodes as a function of the LFP location at various scan rates of 0.05 to 2.0 mV/s in the potential range 2.5 to 4.0 V (vs. Li/Li<sup>+</sup>). The upper insets indicate the linear relationship between the anodic peak current density (mA) at approximately 3.7 V and the square root of the scan rate for the layered electrodes. The lower cartoons represent the multi-layer architecture with varying the LFP location. (d) Corresponding estimates of the effective lithium ion mobility for the LFP layers only. (e) Ragone profiles comparing this work with the literature.

## Graphical abstract

**Hybrid-type positive electrodes exploiting both electrical double layer and intercalation mechanisms** were developed by layer-by-layer spray printing of discrete layers of activated carbon and  $\text{LiFePO}_4$ , producing significant performance benefits in lithium ion capacitors.

High Energy Lithium Ion Capacitors Using Hybrid Cathodes Comprising Electrical Double Layer and Intercalation Host Multi-Layers

Sang Ho Lee\*, Chun Huang and Patrick S. Grant

